Applied Mathematics and Computation 219 (2013) 9947–9958

Contents lists available at SciVerse ScienceDirect

Applied Mathematics and Computation

journal homepage: www.elsevier.com/locate/amc

Structure-preserving Arnoldi-type algorithm for solving eigenvalue problems in leaky surface wave propagation

Tsung-Ming Huang [a], Wen-Wei Lin [b,*], Chin-Tien Wu [b]

[a] Department of Mathematics, National Taiwan Normal University, Taipei 116, Taiwan
[b] Department of Applied Mathematics, National Chiao Tung University, Hsinchu 300, Taiwan

ARTICLE INFO

Keywords:
Leaky SAW
Structure-preserving
Palindromic quadratic eigenvalue problem
GTSHIRA
Mesh refinement

ABSTRACT

We study the generalized eigenvalue problems (GEPs) that arise from modeling leaky surface wave propagation in an acoustic resonator with an infinite amount of periodically arranged interdigital transducers. The constitutive equations are discretized by finite element methods with mesh refinements along the electrode interfaces and corners. The nonzero eigenvalues of the resulting GEP appear in reciprocal pairs $(\lambda, 1/\lambda)$. We transform the GEP into a T-palindromic quadratic eigenvalue problem (TPQEP) to reveal the important reciprocal relationships of the eigenvalues. The TPQEP is then solved by a structure-preserving algorithm incorporating a generalized T-skew-Hamiltonian implicitly restarted Arnoldi method so that the reciprocal relationship of the eigenvalues may be automatically preserved. Compared with applying the Arnoldi method to solve the GEPs, our numerical results show that the eigenpairs produced by the proposed structure-preserving method not only preserve the reciprocal property but also possess high efficiency and accuracy.

© 2013 Elsevier Inc. All rights reserved.

1. Introduction

Waveguide devices have been widely used in controlling and interconnecting guided electromagnetic waves. Advances in thin film technology and efficient transducers further encourage investigations of more sophisticated waveguide concepts in acoustic systems. Acoustic waveguide devices are widely employed in applications including telecommunication filters [8,22] and sensor technologies [2]. One of the basic elements in most of the acoustic wave filters is a resonator that generally consists of reflectors that are externally coupled through two interdigital transducers (IDT) where the first IDT generates the surface waves and the second IDT detects the wave and filters the waves in desired frequency range out. The IDT is primarily made by depositing periodic metallic grating electrodes on a piezoelectric film substrate, as shown in Fig. 1(a). Extensive theoretical and experimental works have been performed, especially on the Rayleigh surface acoustic wave (SAW) [4,9,21,22]. Finite element simulations of piezoelectric devices in two dimensions (2D) and three dimensions (3D) have been studied by Allik and Hughes [1], Buchner et al. [6], Koshiba et al. [16], and Lerch [18] and others. In filter design, it is important to know the stop band width and the center frequency f_c for a given layout of the second sensing IDT, where $f_c = v_s/\lambda_s$ and v_s and λ_s are the wave velocity and the wave length of the incident wave, respectively. The center frequency and stop band width can be determined visually by plotting the dispersion diagram in which an eigenvalue problem associated with each frequency in the search range must be solved.

Because of the slower propagation velocity of the Rayleigh SAW, filters based on Rayleigh SAW design are usually limited to an operational frequency range that is less than 1 GHz. For a frequency higher than 1 GHz, more recent attention has been

* Corresponding author.
E-mail addresses: min@ntnu.edu.tw (T.-M. Huang), wwlin@math.nctu.edu.tw (W.-W. Lin), ctw@math.nctu.edu.tw (C.-T. Wu).

0096-3003/$ - see front matter © 2013 Elsevier Inc. All rights reserved.
http://dx.doi.org/10.1016/j.amc.2013.03.120

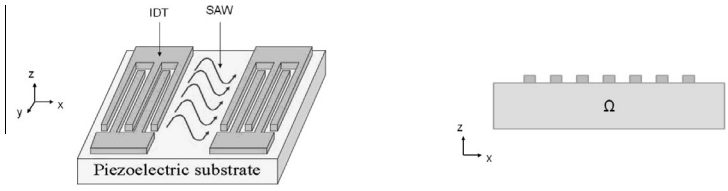

(a) A standard configuration of SAW resonators (b) A 2D model of a LSAW resonator on the sagittal plane

Fig. 1. Sketches of SAW resonators

paid to the so-called leaky surface acoustic wave (LSAW) because of its faster propagation speed in crystal cuts such as 64° YX-$LiNbO_3$ and 36° YX-$LiTaO_3$ and its higher electromechanical coupling and minimal propagation loss in crystal cuts such as 40°–42° YX-$LiTaO_3$ [8]. Searching for a better crystal cut among various piezoelectric substrates (PZT) to increase the LSAW velocity has become one of the major issues in high frequency filter design. For each crystal cut, one must solve many eigenvalue problems to plot the dispersion diagram. An efficient and accurate algorithm for solving eigenvalue problems resulting from the mathematical model of an LSAW resonator is desirable.

The eigenvalue problem [13] obtained from the finite element modeling of the SAW or LSAW resonance can be represented as a T-palindromic quadratic eigenvalue problem (TPQEP) of the form

$$\lambda^2(F^\top M_1^{-1}G)^\top\psi_\ell+\lambda(G^\top M_1^{-1}G+F^\top M_1^{-1}F-M_2)\psi_\ell+(F^\top M_1^{-1}G)\psi_\ell=0, \tag{1}$$

or a generalized eigenvalue problem (GEP) of the form

$$\begin{bmatrix}M_1 & G\\ F^\top & 0\end{bmatrix}\begin{bmatrix}\psi_i\\ \psi_\ell\end{bmatrix}+\lambda\begin{bmatrix}0 & F\\ G^\top & M_2\end{bmatrix}\begin{bmatrix}\psi_i\\ \psi_\ell\end{bmatrix}=0, \tag{2}$$

where $M_1^\top=M_1\in\mathbb{C}^{n\times n}$, $M_2^\top=M_2\in\mathbb{C}^{m\times m}$, F and $G\in\mathbb{C}^{n\times m}$ with $m\ll n$, and the superscript "$\top$" denotes the complex transpose. The scalar $\lambda\in\mathbb{C}$ is called the eigenvalue of (1) and (2), and the nonzero vectors ψ_ℓ and $\begin{bmatrix}\psi_i^\top & \psi_\ell^\top\end{bmatrix}^\top$ are the associated eigenvectors of (1) and (2), respectively. It is easily seen from (1) that the eigenvalues appear in reciprocal pairs $(\lambda,1/\lambda)$ (including 0 and ∞).

The TPQEP (1) can be linearized as a GEP. The linearized GEP, as well as the GEP (2), is then solved by traditional methods such as the QZ algorithm [13] or Arnoldi method. However, the reciprocal property of the eigenvalues can be easily destroyed, and large numerical errors can be generated during the computation [15]. To preserve the reciprocal property of the eigenvalues, a structure-preserving doubling algorithm for solving the TPQEP was developed in [11] via the computation of a solvent of a nonlinear matrix equation. Another structure-preserving algorithm based on the $(\mathcal{S}+\mathcal{S}^{-1})$-transform [19] and Patel's approach [24] was developed in [14]. The drawback of solving (1) by using these structure-preserving algorithms is that they need to explicitly compute the coefficient matrices in (1) which require large computational costs. To remedy these drawbacks, we transform the GEP (2) into a new TPQEP of the form

$$\mathcal{P}(\lambda)\psi_i\equiv(\lambda^2A_1^\top+\lambda A_0+A_1)\psi_i=0 \tag{3a}$$

with

$$A_1^\top=FM_2^{-1}G^\top,\quad A_0=FM_2^{-1}F^\top+GM_2^{-1}G^\top-M_1 \tag{3b}$$

so that the structure-preserving algorithm [14] using the $(\mathcal{S}+\mathcal{S}^{-1})$-transform and the generalized T-skew-Hamiltonian implicitly restarted Arnoldi method (GTSHIRA) can be applied to search eigenvalues in a specified region of interest. On the basis of the shift-and-invert technique, the desired eigenpairs can be easily extracted. For giving a shift value τ, in each iteration of GTSHIRA, the shift-and-invert technique leads to solve a linear system $(\tau^2A_1^\top+\tau A_0+A_1)x=b$. From (3b), although the coefficient matrices A_0 and A_1 are large, they are not sparse. In order to avoid the computations of A_0 and A_1 in (3b), we apply the Sherman–Morrison–Woodbury formula to directly solve the linear system. Compared with the traditional Arnoldi method for solving GEP (2), our proposed structure-preserving method not only preserves the reciprocal property but also possesses a high efficiency and accuracy.

This paper is organized as follows. We first introduce finite element modeling for a simple resonator in Section 2. In Section 3, we introduce the efficient structure-preserving algorithm to solve the large and sparse generalized eigenvalue problems resulting from our FEM model. Our numerical experiments in Section 4 show that the proposed structure-preserving algorithm for solving the GEP in (2) is efficient and accurate. Finally, we conclude this paper in Section 5.

2. Finite element model for SAW

In contrast to the well-known Rayleigh waves, which consist of partial longitudinal waves and shear waves, the LSAW propagates mainly in the shear direction on the sagittal plane and is trapped at the substrate surface and satisfies the

stress-free boundary condition on the surface. These properties allow one to reduce the general mode analysis in 3D to a 2D problem, as shown in Fig. 1(b) [25]. Furthermore, the boundary conditions for displacement can naturally be set to be rigid on the bottom boundary and stress-free on the top surface, and the boundary conditions for the electric potential can be set to be short-circuited for the electrodes on the top boundary and open-circuited elsewhere [10]. As proved in Auld's book [4], these boundary conditions guarantee mode orthogonality and further ensure that the mode excitation is determined by the applied traction force and the potential on the free surface. Therefore, on the sagittal plane, the usual 2D mode analysis can be applied to analyze the LSAW on the resonators with IDTs. In the following, we consider only the LSAW resonator on a 2D plane (the sagittal plane associated with the crystal cuts).

To model the wave propagation in an infinite domain with periodically arranged electrodes because of the Floquet–Bloch Theorem, we can reduce the problem to a single cell domain with one IDT by assuming that the wave ψ is quasi-periodic of the form $\psi(x_1,x_2)=\psi_p(x_1,x_2)e^{(\alpha+i\beta)x_1}$, where x_1 is the wave propagation direction, p is the length of the unit cell (i.e., the periodic interval), α and β are the attenuation and phase shifts along the wave propagation direction, respectively, and ψ_p satisfies $\psi_p(x_1+p,x_2)=\psi_p(x_1,x_2)$. Let Ω denote the piezoelectric transducer with a single IDT as shown in Fig. 2, and let Γ_l and Γ_r denote the left and right boundary segments of Ω. For the general anisotropic PZT substrates, under the assumption of linear piezoelectric coupling, the elastic and electric fields interact following the general material constitutions below:

$$\begin{aligned} T &= c^E S - e^\top E, \\ D &= eS + \varepsilon^S E, \end{aligned} \tag{4}$$

where vectors T,S,D and E are the mechanical stress, strain, dielectric displacement and electric field, respectively, and the matrices c^E,ε^S and e are the elasticity constant, the dielectric constant and the piezoelectric constant matrices, respectively, measured at constant electric and constant strain fields at a constant temperature. For various crystal cut of the PZT, the material constant matrices c^E,ε^S and e depend on the Euler angle θ of the cut. By applying the Bond strain transformation matrix N_θ [5] and the usual coordinates transformation matrix M_θ to the strain field and electric field, respectively, the material constant matrices for the cut angle θ can be obtained by

$$c^E := [N_\theta]^\top c_0^E[N_\theta], \quad e := [M_\theta]^\top e_0[N_\theta], \quad \text{and} \quad \varepsilon^S := [M_\theta]^\top \varepsilon_0^S[M_\theta],$$

here c_0^E, e_0, and ε_0^S denote the material constant matrices of the crystal cut at Euler angle $\theta=[0^\circ,0^\circ,0^\circ]$.

By applying the virtual work principle to Eq. (4), the equilibrium state under the external body force f, the electrical field g and the above mentioned boundary conditions of the LSAW resonator, we have

$$\begin{aligned} &\int_\Omega [\delta S]^\top C^E[S]\,dV + \int_\Omega [\delta S]^\top e^\top [\nabla\phi]\,dV + \int_\Omega [\nabla\delta\phi]^\top e[S]\,dV - \int_\Omega [\nabla\delta\phi]^\top \varepsilon^S[\nabla\phi]\,dV + \int_\Omega \delta q^\top \rho\ddot{q}\,dV \\ &= \int_\Omega \delta q^\top f\,dV + \int_\Omega [\nabla\delta\phi]^\top g\,dV + \int_{\Gamma_l\cup\Gamma_r} \delta q^\top (T\cdot\vec{n})\,dA + \int_{\Gamma_l\cup\Gamma_r} \delta\phi^\top (D\cdot\vec{n})\,dA. \end{aligned} \tag{5}$$

Here, ρ is the mass density, $\vec{n}$ is the boundary normal, $q=[u,v,w]^\top$ is the displacement vector, ϕ is the electric potential that satisfies $\nabla\phi=E$, $S=[\frac{\partial u}{\partial x},\frac{\partial v}{\partial y},\frac{\partial w}{\partial z},\frac{\partial v}{\partial z}+\frac{\partial w}{\partial y},\frac{\partial w}{\partial x}+\frac{\partial u}{\partial z},\frac{\partial u}{\partial y}+\frac{\partial v}{\partial x}]^\top$, and δq, $\delta\phi$ and δS are the corresponding virtual displacement, potential and strain vectors, respectively. The equation can then be discretized by finite element method [1,10]. Following the usual free mode analysis, we consider $f=0, g=0$ and a time harmonic quasi periodic solution vector $\psi_\omega(x,t)=\psi(x)e^{i\omega t}$. The spatial function $\psi(x)=[q(x),\phi(x)]$ satisfies the boundary conditions shown in Fig. 2 in which the periodic boundary conditions, proposed by Buchner [6],

$$\psi_r = \psi(x_1+p,x_2) = \gamma\psi(x_1,x_2) = \gamma\psi_l, \tag{6}$$

$$T_r\cdot n_r = T(\psi_r)\cdot n_r = -\gamma T(\psi_l)\cdot n_l = -\gamma T_l\cdot n_l, \tag{7}$$

$$D_r\cdot n_r = D(\psi_r)\cdot n_r = -\gamma D(\psi_l)\cdot n_l = -\gamma D_l\cdot n_l, \tag{8}$$

are enforced on the left and right boundaries, Γ_l and Γ_r, here n_l and n_r are the normal vector of Γ_l and Γ_r respectively and $\gamma=e^{-(\alpha+i\beta)}$. By plugging ψ_w into (5), the equation can be rewritten in the following matrix form:

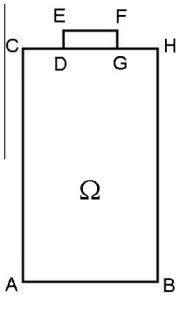

Boundary conditions on boundary segments Γ_s:

Open circuit condition $D\cdot\vec{n}=0$ on $\Gamma_s=\overline{AB},\overline{CD},\overline{GH}$

Short circuit condition $\phi|_{\Gamma_s}=g_s$ on $\Gamma_s=\overline{DE},\overline{EF},\overline{FG}$

Stress free condition $T\cdot\vec{n}=0$ on $\Gamma_s=\overline{CD},\overline{DE},\overline{EF},\overline{FG},\overline{GH}$

Rigid boundary condition $q|_{\Gamma_s}=0$ on $\Gamma_s=\overline{AB}$

$\Gamma_l=\overline{AC}$, $\Gamma_r=\overline{BH}$

Fig. 2. A 2D single cell domain of a LSAW resonator and boundary conditions where the region DEFG is a aluminium electrode and the region ACHB is the PZT substrate.

$$\begin{bmatrix} K^{qq}-\omega^2 M^{qq} & K^{q\phi} \\ K^{\phi q} & -K^{\phi\phi} \end{bmatrix} \begin{bmatrix} q \\ \phi \end{bmatrix} = \begin{bmatrix} F_l + F_r \\ Q_l + Q_r \end{bmatrix}, \tag{9}$$

where

$$K^{qq} = \int_\Omega \delta q^\top B_S^\top C^E B_S q \, dV, \quad M^{qq} = \int_\Omega \delta q^\top \rho q \, dV, \quad \text{and} \quad K^{\phi\phi} = \int_\Omega \delta\phi^\top B_\phi^\top e B_S q \, dV,$$

$$K^{q\phi} = \int_\Omega \delta q^\top B_S^\top e^\top B_\phi \phi \, dV \quad \text{and} \quad K^{\phi q} = \int_\Omega \delta\phi^\top B_\phi^\top e B_S q \, dV,$$

$$F_l = \int_{\Gamma_l} \delta q^\top T_l \vec{n}_l \, dA \quad \text{and} \quad F_r = \int_{\Gamma_r} \delta q^\top T_r \vec{n}_r \, dA,$$

$$Q_l = \int_{\Gamma_l} \delta\phi^\top D_l \vec{n}_l \, dA \quad \text{and} \quad Q_r = \int_{\Gamma_r} \delta\phi^\top D_r \vec{n}_r \, dA,$$

and the matrices $B_S = \begin{bmatrix} \frac{\partial}{\partial x} & 0 & 0 & 0 & \frac{\partial}{\partial z} & \frac{\partial}{\partial y} \\ 0 & \frac{\partial}{\partial y} & 0 & \frac{\partial}{\partial z} & 0 & \frac{\partial}{\partial x} \\ 0 & 0 & \frac{\partial}{\partial z} & \frac{\partial}{\partial y} & \frac{\partial}{\partial x} & 0 \end{bmatrix}^\top$ and $B_\phi = \begin{bmatrix} \frac{\partial}{\partial x} & \frac{\partial}{\partial y} & \frac{\partial}{\partial z} \end{bmatrix}^\top$. Mechanical damping effects can also be considered by using the Rayleigh damping assumption in which the matrix $K^{qq}-\omega^2 M^{qq}$ in (9) are modified into $K^{qq} + i\omega(\kappa_1 K^{qq} + \kappa_2 M^{qq}) - \omega^2 M^{qq}$. Here κ_1 and κ_2 are coefficients associated with the viscous damping and mass damping, respectively.

To obtain the generalized eigenvalue problem that is associated with the propagation parameter γ, following Hofer's approach [13], the nodal unknowns are split into the inner nodes $\psi_i = [q_i, \phi_i]$, the left boundary nodes $\psi_l = [q_l, \phi_l]$ and the right boundary nodes $\psi_r = [q_r, \phi_r]$. The matrix Eq. (9) can be recast into the following form:

$$\begin{bmatrix} K_{ii} & K_{il} & K_{ir} \\ K_{li} & K_{ll} & K_{lr} \\ K_{ri} & K_{rl} & K_{rr} \end{bmatrix} \begin{bmatrix} \psi_i \\ \psi_l \\ \psi_r \end{bmatrix} = \begin{bmatrix} 0 \\ R_l \\ R_r \end{bmatrix}, \tag{10}$$

where R_l and R_r are vectors obtained from the discretization of the terms $F_l + Q_l$ and $F_r + Q_r$, respectively. From the periodic boundary conditions (6), (7) and (8), (10) becomes the following:

$$\begin{bmatrix} K_{ii} & K_{il} & K_{ir} \\ K_{li} & K_{ll} & K_{lr} \\ K_{ri} & K_{rl} & K_{rr} \end{bmatrix} \begin{bmatrix} I_i & 0 \\ 0 & I_l \\ 0 & \gamma I_l \end{bmatrix} \begin{bmatrix} \psi_i \\ \psi_l \end{bmatrix} = \begin{bmatrix} 0 \\ I_l \\ -\gamma I_l \end{bmatrix} R_l. \tag{11}$$

Furthermore, by multiplying the matrix

$$\begin{bmatrix} I_i & 0 & 0 \\ 0 & \gamma I_l & I_l \end{bmatrix}$$

with (11), the GEP associated with the propagation parameter γ is obtained:

$$\left(\begin{bmatrix} K_{ii} & K_{il} \\ K_{ir}^\top & 0 \end{bmatrix} + \gamma \begin{bmatrix} 0 & K_{ir} \\ K_{il}^\top & K_{ll} + K_{rr} \end{bmatrix} \right) \begin{bmatrix} \psi_i \\ \psi_l \end{bmatrix} = 0. \tag{12}$$

Because the viscosity is small for most crystalline solids, the attenuation factor α is close to zero. As a result, the propagation factors λ near the unit circle, denoted by $\mathbb{U}$, are desired. Moreover, for the frequency ω in the stopping band, the frequency shift parameter β will be close to π when the periodic interval p (i.e., the domain width here) equals half of the incident wave length λ_0. Therefore, for the eigenvalue problem (12), we are interested in finding the eigenvalues λ that are close to $\mathbb{U}$, especially, those that are near -1 on the complex plane.

Note that it is well known that the solution of a general elliptic problem has singularities near to corners [12], and in addition, the solution can become less regular near the interface between the electrode and the PZT substrate. It is inevitable that the error from discretization could be amplified when the reciprocal pairs of eigenvalues are computed. Therefore, it is important to minimize the accuracy deterioration from singularities and low regularity in finite element solutions. One can resolve the singularity by constructing the singular elements in which the mesh points are clustered to the singular source according to the order of the singularity [3]. In our calculation, we simply employ locally refined meshes. An additional benefit from using locally refined meshes is that we can discretize Eq. (9) using linear elements instead of using high order finite element discretization [6]. Due to the simple discretization scheme on locally refined meshes, the GEP becomes very large sparse, an accurate and robust eigensolver for preserving the reciprocal eigenpair structure is needed. We present our algorithm and numerical results in the following sections.

3. Structure-preserving Arnoldi-type algorithm

Observing that the imaginary part of $K_{ll} + K_{rr}$ in (12) is symmetric and positive definite, by the Bendixson Theorem, $K_{ll} + K_{rr}$ is invertible. The second equation of (12) gives

$$\psi_l = -\frac{1}{\gamma}(K_{ll}+K_{rr})^{-1}K_{ir}^{\top}\psi_i - (K_{ll}+K_{rr})^{-1}K_{il}^{\top}\psi_i. \tag{13}$$

Letting

$$M_1 = K_{ii}, \quad M_2 = K_{ll}+K_{rr}, \quad F = K_{ir}, \quad G = K_{il}, \quad x = \psi_i, \quad \lambda = \gamma, \tag{14}$$

and substituting (13) into the first equation of (12), we obtain the TPQEP in (3). To solve (3) in a structure-preserving way, we first transform the TPQEP in (3a) into a $\top$-skew-Hamiltonian pencil $(\widehat{\mathcal{K}},\widehat{\mathcal{N}})$ through the following procedure:

1. The TPQEP is linearized into a special GEP [14],
$$(\mathcal{M}-\lambda\mathcal{L})\begin{bmatrix}x\\ y\end{bmatrix} = 0, \tag{15}$$
where $\lambda y = A_1 x$, and
$$\mathcal{M} = \begin{bmatrix}A_1 & 0\\ -A_0 & -I\end{bmatrix}, \quad \mathcal{L} = \begin{bmatrix}0 & I\\ A_1^{\top} & 0\end{bmatrix}. \tag{16}$$
The reciprocal eigenpairs $(\lambda, 1/\lambda)$ are kept in the matrix pencil $(\mathcal{M},\mathcal{L})$ because the matrix pencil $\mathcal{M}-\lambda\mathcal{L}$ is $\top$-symplectic, i.e., it satisfies $\mathcal{M}\mathcal{J}\mathcal{M}^{\top} = \mathcal{L}\mathcal{J}\mathcal{L}^{\top}$ where $\mathcal{J} = \begin{bmatrix}0 & I_n\\ -I_n & 0\end{bmatrix}$.
2. Using the $(\mathcal{S}+\mathcal{S}^{-1})$-transform, the matrix pencil $\mathcal{M}-\lambda\mathcal{L}$ is further transformed to a $\top$-skew-Hamiltonian pencil $\mathcal{K}-\mu\mathcal{N}$, i.e., $(\mathcal{K}\mathcal{J})^{\top} = -\mathcal{K}\mathcal{J}$, $(\mathcal{N}\mathcal{J})^{\top} = -\mathcal{N}\mathcal{J}$ and μ is the eigenvalue of the pencil:
$$\mathcal{K}-\mu\mathcal{N} \equiv [(\mathcal{L}\mathcal{J}\mathcal{M}^{\top} + \mathcal{M}\mathcal{J}\mathcal{L}^{\top}) - \mu\mathcal{L}\mathcal{J}\mathcal{L}^{\top}]\mathcal{J}^{\top}. \tag{17}$$
From the relationship $\mu = \lambda + 1/\lambda$, one can relate the two eigenvalues λ and μ and further implies that the multiplicity of the eigenvalue μ is even.
3. Let τ be a shift value and $\tau \notin \sigma(\mathcal{M},\mathcal{L})$ where $\sigma(\mathcal{A},\mathcal{B})$ denotes the set of all eigenvalues of any matrix pair $(\mathcal{A},\mathcal{B})$. Since $\mu_0 \equiv \tau + 1/\tau \notin \sigma(\mathcal{K},\mathcal{N})$, one can define the shift–invert transformation $\widehat{\mathcal{K}}-\widehat{\mu}\widehat{\mathcal{N}}$ for $\mathcal{K}-\mu\mathcal{N}$ with $\widehat{\mu} = (\mu-\mu_0)^{-1}$ where
$$\widehat{\mathcal{K}} \equiv -\tau\mathcal{N} = \tau\begin{bmatrix}A_1^{\top} & 0\\ 0 & A_1\end{bmatrix}, \tag{18a}$$
$$\widehat{\mathcal{N}} \equiv -\tau(\mathcal{K}-\mu_0\mathcal{N}) = (\mathcal{M}-\tau\mathcal{L})\mathcal{J}(\mathcal{M}^{\top}-\tau\mathcal{L}^{\top})\mathcal{J}^{\top}, \tag{18b}$$
and $\widehat{\mathcal{K}}$ and $\widehat{\mathcal{N}}$ are $\top$-skew-Hamiltonian.

The relationship between eigenpairs of the TPQEP in (3) and the $\top$-skew-Hamiltonian pencil $(\widehat{\mathcal{K}},\widehat{\mathcal{N}})$ in (18) is stated in the following theorem.

Theorem 3.1 [14]. *Let $(\widehat{\mathcal{K}},\widehat{\mathcal{N}})$ be defined in (3) and τ be a shift value with $\tau \notin \sigma(\mathcal{M},\mathcal{L})$. If $(\widehat{\mu},[z_1^{\top},z_2^{\top}]^{\top})$ with $z_1,z_2 \in \mathbb{C}^n$ is an eigenpair of $(\widehat{\mathcal{K}},\widehat{\mathcal{N}})$ and ν satisfies $\tau + \frac{1}{\tau} + \frac{1}{\widehat{\mu}} = \nu + \frac{1}{\nu}$, then $z_1 + \frac{1}{\nu}z_2$ and $z_1 + \nu z_2$ are eigenvectors of the TPQEP in (3) corresponding to eigenvalues ν and $\frac{1}{\nu}$, respectively.*

From the definition of $\widehat{\mathcal{N}}$ in (18b), $\widehat{\mathcal{N}}$ can be factorized as $\widehat{\mathcal{N}} = \mathcal{N}_1\mathcal{N}_2$, where
$$\mathcal{N}_1 = \mathcal{M}-\tau\mathcal{L}, \quad \mathcal{N}_2 = \mathcal{J}(\mathcal{M}^{\top}-\tau\mathcal{L}^{\top})\mathcal{J}^{\top} \tag{19}$$
are nonsingular and satisfy $\mathcal{N}_2^{\top}\mathcal{J} = \mathcal{J}\mathcal{N}_1$.Let $\mathcal{B} \equiv \mathcal{N}_1^{-1}\widehat{\mathcal{K}}\mathcal{N}_2^{-1}$ and u_1 be an initial vector. Define the Krylov matrix with respect to u_1 by
$$K_n \equiv K_n[\mathcal{B},u_1] = [u_1, \mathcal{B}u_1, \ldots, \mathcal{B}^{n-1}u_1].$$

Theorem 3.2 guarantees that the Arnoldi process can be executed in a way that the $\top$-skew-Hamiltonian structure of the matrix pencil is preserved. As a result, a generalized $\top$-skew-Hamiltonian implicitly restarted Arnoldi (GTSHIRA) algorithm proposed in [14] can be employed to solve the eigenvalue problem $\widehat{\mathcal{K}}z = \widehat{\mu}\widehat{\mathcal{N}}z$.

Theorem 3.2 [14]. *Let $\mathcal{B} = \mathcal{N}_1^{-1}\widehat{\mathcal{K}}\mathcal{N}_2^{-1}$ with $\widehat{\mathcal{N}} = \mathcal{N}_1\mathcal{N}_2$ be $\top$-skew-Hamiltonian and $K_n \equiv K_n[\mathcal{B},u_1]$ be the Krylov matrix with rank$(K_n) = n$. Then there are unitary matrices $\mathcal{U}$ and $\mathcal{V}$ satisfying $\mathcal{V} = \mathcal{J}^{\top}\mathcal{U}\mathcal{J}$, $\mathcal{U}e_1 = u_1$ and $\mathcal{V}e_1 = \mathcal{N}_1u_1/\|\mathcal{N}_1u_1\|_2$ such that*
$$\mathcal{V}^{\top}\widehat{\mathcal{K}}\mathcal{U} = \begin{bmatrix}\widehat{H}_n & \widehat{S}_n\\ 0 & \widehat{H}_n^{\top}\end{bmatrix}, \quad \mathcal{V}^{\top}\widehat{\mathcal{N}}\mathcal{U} = \begin{bmatrix}\widehat{R}_n & \widehat{T}_n\\ 0 & \widehat{R}_n^{\top}\end{bmatrix}, \tag{20}$$
where $\widehat{H}_n$ is unreduced upper Hessenberg, $\widehat{R}_n$ is nonsingular upper triangular and $\widehat{S}_n,\widehat{T}_n$ are $\top$-skew-symmetric.

The unitary matrices $\mathcal{U}$ and $\mathcal{V}$ in Theorem 3.2 can be generated in a structure-preserving way (GTSHIRA) as follows. Recall that the $\top$-bi-isotropic orthonormal matrices $\widehat{Z}_j, \widehat{Y}_j \in \mathbb{C}^{2n\times j}$ are computed iteratively according to the following structure-preserving Arnoldi process:

$$\widehat{\mathcal{K}}\widehat{Z}_j = \widehat{Y}_j\widehat{H}_j + \widehat{h}_{j+1,j}\widehat{y}_{j+1}e_j^\top \tag{21}$$

and

$$\widehat{\mathcal{N}}\widehat{Z}_j = \widehat{Y}_j\widehat{R}_j \tag{22}$$

with

$$\widehat{Y}_j^H\widehat{y}_{j+1} = 0 \quad \text{and} \quad \widehat{Z}_j^\top\mathcal{J}\widehat{y}_{j+1} = 0, \tag{23}$$

where $\widehat{H}_j, \widehat{R}_j \in \mathbb{C}^{j\times j}$ are unreduced upper Hessenberg and nonsingular upper triangular, respectively. By defining $\mathcal{U}_j \equiv [\widehat{Z}_j, -\mathcal{J}\bar{\widehat{Y}}_j]$ and $\mathcal{V}_j \equiv [\bar{\widehat{Y}}_j, -\mathcal{J}\widehat{Z}_j]$ where $\bar{\widehat{Y}}_j$ denotes the conjugate matrices of $\widehat{Y}_j$, it is easily seen that

$$\mathcal{V}_j^\top\widehat{\mathcal{K}}\mathcal{U}_j = \begin{bmatrix} \widehat{H}_j & -\widehat{Y}_j^H\widehat{\mathcal{K}}\mathcal{J}\bar{\widehat{Y}}_j \\ 0 & \widehat{H}_j^\top \end{bmatrix}, \quad \mathcal{V}_j^\top\widehat{\mathcal{N}}\mathcal{U}_j = \begin{bmatrix} \widehat{R}_j & -\widehat{Y}_j^H\widehat{\mathcal{N}}\mathcal{J}\bar{\widehat{Y}}_j \\ 0 & \widehat{R}_j^\top \end{bmatrix}$$

which implies that the $\top$-skew-Hamiltonian property is preserved in each iteration step.

Note that Theorem 3.1 indicates that although the number of the eigenvectors associated with the eigenvalue μ is even, only half of the eigenvectors are needed to extract all the eigenvectors corresponding to the eigenvalues v and $\frac{1}{v}$. Furthermore, through the above mentioned structure-preserving Arnoldi process, the $\top$-skew-Hamiltonian structure of the matrix pencil in Theorem 3.2 is preserved and the even multiplicity of the eigenvalue μ is automatically obtained. Therefore, the required halves of the eigenvectors associated with the eigenvalue μ can be easily computed when the desired eigenpairs are convergent. In fact, the desired eigenpairs $(\widehat{\mu}_i, z_i)$ of $(\widehat{\mathcal{K}}, \widehat{\mathcal{N}})$ can be computed from the matrix pair $(\widehat{H}_j, \widehat{R}_j)$ with $\widehat{H}_j\hat{s}_i = \widehat{\mu}_i\widehat{R}_j\hat{s}_i$ and $z_i = \widehat{Z}_j\hat{s}_i$. From Theorem 3.1, one can compute the desired eigenpairs of $(\mathcal{M}, \mathcal{L})$ from $(\widehat{\mu}_i, z_i)$ and preserve the reciprocal relationship of the eigenvalues of the GEP algebraically.

We summarize the above procedures for computing the reciprocal eigenpairs of the GEP (12) in Algorithm 1. Note that, in step 1 of Algorithm 1, the linear systems

$$\mathcal{N}_1 v_1 = b_1, \quad \mathcal{N}_2 v_2 = b_2, \tag{24}$$

have to be solved in order to obtain $\widehat{Z}_j$ from (22). This is indeed the most time-consuming step in the proposed structure-preserving algorithm. In the following, we discuss how to solve (24) efficiently.

Algorithm 1. Structure-preserving algorithm for solving GEP (12)

Input: matrices F, G, M_2 and M_1, shift value τ and the number $\mathfrak{m}$ of desired eigenvalues.

Output: eigenpairs $\{(\gamma_j, [(\psi_{ij}^{(1)})^\top, (\psi_{lj}^{(1)})^\top]^\top), (\gamma_j^{-1}, [(\psi_{ij}^{(2)})^\top, (\psi_{lj}^{(2)})^\top]^\top)\}_{j=1}^{\mathfrak{m}}$ of the GEP in (12) where $\gamma_j + \gamma_j^{-1}$ for $j = 1, \ldots, \mathfrak{m}$ are the closest to shift value $\tau + \tau^{-1}$.

1: Compute eigenpairs $\{(\widehat{\mu}_j, z_j \equiv [z_{j1}^\top, z_{j2}^\top]^\top)\}_{j=1}^{\mathfrak{m}}$ of $(\widehat{\mathcal{K}}, \widehat{\mathcal{N}})$ by using GTSHIRA.

2: Compute eigenvalues γ_j and $\frac{1}{\gamma_j}$ of TPQEP in (3) by solving

$$\gamma^2 - (\tau + \tau^{-1} + \widehat{\mu}_j^{-1})\gamma + 1 = 0;$$

Compute eigenvectors

$$\psi_{ij}^{(1)} \equiv \frac{1}{\gamma_j}z_{j1} - z_{j2}, \quad \psi_{ij}^{(2)} \equiv \gamma_j z_{j1} - z_{j2}$$

corresponding to $\gamma_j, \frac{1}{\gamma_j}$, respectively, for $j = 1, 2, \ldots, \mathfrak{m}$.

3: Compute

$$\psi_{lj}^{(1)} = -M_2^{-1}(\gamma_j^{-1}F^\top\psi_{ij}^{(1)} + G^\top\psi_{ij}^{(1)}), \ \psi_{lj}^{(2)} = -M_2^{-1}(\gamma_j F^\top\psi_{ij}^{(2)} + G^\top\psi_{ij}^{(2)})$$

for $j = 1, \ldots, \mathfrak{m}$.

By the definitions of $\mathcal{M}$ and $\mathcal{L}$ in (16), we have

$$\begin{bmatrix} I & -\tau I \\ 0 & I \end{bmatrix}(\mathcal{M}-\tau\mathcal{L}) = \begin{bmatrix} \tau^2 A_1^\top + \tau A_0 + A_1 & 0 \\ -A_0 - \tau A_1^\top & -I \end{bmatrix} \tag{25a}$$

and

$$\begin{bmatrix} I & -A_0 - \tau A_1 \\ 0 & I \end{bmatrix}(\mathcal{M}^\top-\tau\mathcal{L}^\top) = \begin{bmatrix} \tau^2 A_1 + \tau A_0 + A_1^\top & 0 \\ -\tau I & -I \end{bmatrix}. \tag{25b}$$

From (19) and (25), we see that solving (24) is equivalent to solving

$$\begin{aligned} &(\tau^2 A_1^\top + \tau A_0 + A_1)v_{11} = b_{11} - \tau b_{12}, \\ &v_{12} = -b_{12} - (A_0 + \tau A_1^\top)v_{11}, \end{aligned} \tag{26}$$

and

$$\begin{aligned} &(\tau^2 A_1 + \tau A_0 + A_1^\top)v_{22} = b_{22} + (A_0 + \tau A_1)b_{21}, \\ &v_{21} = \tau v_{22} - b_{21}, \end{aligned} \tag{27}$$

where $v_1 = [v_{11}^\top, v_{12}^\top]^\top$, $v_2 = [v_{21}^\top, v_{22}^\top]^\top$, $b_1 = [b_{11}^\top, b_{12}^\top]^\top$ and $b_2 = [b_{21}^\top, b_{22}^\top]^\top$. By the definitions of A_0 and A_1, it holds that

$$\tau^2 A_1^\top + \tau A_0 + A_1 = (G + \tau F)M_2^{-1}(F^\top + \tau G^\top) - \tau M_1 \tag{28}$$

and

$$\tau^2 A_1 + \tau A_0 + A_1^\top = (F + \tau G)M_2^{-1}(G^\top + \tau F^\top) - \tau M_1. \tag{29}$$

Let $M_1 = LU$ be the LU factorization of M_1. Set

$$E_1 = L^{-1}\left(\frac{1}{\tau}G + F\right), \quad E_2 = U^{-\top}(F + \tau G).$$

By the Sherman–Morrison–Woodbury formula, (28) and (29) can be further factorized as following,

$$(\tau^2 A_1^\top + \tau A_0 + A_1)^{-1} = -\frac{1}{\tau}U^{-1}[I - E_1 M_2^{-1}E_2^\top]^{-1}L^{-1} = -\frac{1}{\tau}U^{-1}[I + E_1(M_2 - E_2^\top E_1)^{-1}E_2^\top]L^{-1}, \tag{30}$$

and

$$(\tau^2 A_1 + \tau A_0 + A_1^\top)^{-1} = -\frac{1}{\tau}L^{-\top}[I + E_2(M_2 - E_1^\top E_2)^{-1}E_1^\top]U^{-\top}. \tag{31}$$

Now, obviously, the solutions of (26) and (27) can be obtained by two forward substitutions (L^{-1}), two backward substitutions (U^{-1}) and solving small linear systems $(M_2 - E_2^\top E_1)^{-1}$ and $(M_2 - E_1^\top E_2)^{-1}$. As a result, Algorithm 1 is very efficient.

4. Numerical results

In this section, we first conduct numerical results to validate the convergence of our finite element model. Second, we report numerical comparisons with our structure-preserving method and the traditional Arnoldi method for solving the GEP (12) to demonstrate the accuracy and efficiency of the proposed eigenvalue solver. All of the computations are performed in MATLAB 2010b on an HP workstation with an Intel Quad-Core Xeon X5570 2.93 GHz and 60 GB of main memory, using IEEE double-precision floating-point arithmetic.

The configuration of our computational domain, shown in Fig. 2, is as follows. The domain width $\overline{AB}$ and the height $\overline{CD}$ are set to be 10^{-6} and 3×10^{-6}, respectively. The ratio of the electrode width $\overline{EF}$ versus the domain width is set to be $\frac{1}{2}$ and the ratio of the electrode thickness $\overline{DE}$ versus the domain height is $\frac{1}{15}$. The material constants of $LiTaO_3$ and $LiNbO_3$ are taken from the measurements obtained by Kushibiki, Takanaga and Sannomiya [17]. Additionally, the viscous damping coefficient $\kappa_1 \approx O(10^{-8})$ in the 10 KHZ operation range and $\kappa_1 \approx O(10^{-10})$ in the MHZ operation range for a family of PZT materials has been shown in [20,23]. In general, κ_1 depends on the operation frequency ω. The viscous damping coefficient is extrapolated to the GHz operation range according to the reciprocal rule $\kappa_1 \propto \frac{1}{\omega}$ [7]. In our numerical studies, the viscous damping coefficient κ_1 is set to be 10^{-14}, and the mass damping coefficient κ_2 is taken as $1 - \kappa_1$ to account for the effect of the electrode weight.

4.1. Accuracy and convergence of finite element approximation

First, we show that our finite element model gives accurate results when predicting the center of the stopping band of LSAW on the filters with aluminum electrodes on top of the piezoelectric substrates 36° YX-$LiTaO_3$ and 64°

YX-$LiNbO_3$. The dispersion diagrams of the attenuation constant α and the propagation constant β associated with the eigenvalue $\lambda(\omega)$, which is the closest to -1 on the complex plane for the frequency ω around the stopping bands, are shown in Fig. 3(a) and (b) for the crystals 36° YX-$LiTaO_3$ and 64° YX-$LiNbO_3$, respectively. A typical shear wave displacement associated with the eigenvector of the computed eigenvalue is shown in Fig. 4 which mesh is locally refined twice near the interface over a uniform mesh.

To measure the convergence of the eigenvalues, tests over three successively refined meshes with an initial mesh length of $h = \frac{p}{20}$ are performed. The dimensions of matrices M_1 and M_2 associated with uniform meshes and locally refined meshes are listed in the second and third columns of Table 1, respectively. We set $\lambda_{[i,\xi]}$ to be the eigenvalue obtained from the meshes with a mesh length of $p/(10 \times i)$. Here, the index $\xi = u$ and $\xi = \ell$ denote that the mesh is uniform without and with local refinement, respectively. Using $\lambda_{[16,u]}$ as an exact value, the convergence of the eigenvalues can be verified from $|\lambda_{[16,u]} - \lambda_{[2^i,u]}|$ and $|\lambda_{[16,u]} - \lambda_{[2^i,\ell]}|$ for $i = 1, 2, 3$. The values of $|\lambda_{[16,u]} - \lambda_{[2^i,u]}|$ and $|\lambda_{[16,u]} - \lambda_{[2^i,\ell]}|$ $(i = 1, 2, 3)$ for 36° YX-$LiTaO_3$ and 64° YX-$LiNbO_3$ at ω_s and ω_e are shown in Table 2, where ω_s and ω_e are the frequencies for which the stopping band starts and ends, respectively. From Table 2, it can be seen that the accuracy of the eigenvalue is increased as the mesh length is reduced and is improved with locally refined meshes. The average of the error reduction rate is about 3.68 which is calculated by averaging the ratio $\frac{|\lambda_{[16,u]} - \lambda_{[2^i,u]}|}{|\lambda_{[16,u]} - \lambda_{[2^{i+1},u]}|}$, for $i = 1, 2$, over both cases. Moreover, it is known that the wave propagation velocity is approximately 4112 m/s for 36° YX-$LiTaO_3$ and approximately 4478 m/s for 64° YX-$LiNbO_3$. It is clear that because the domain width $p = 1 \times 10^{-6}$, the center of the stopping band is approximately 2.056 GHz and 2.239 GHz for 36° YX-$LiTaO_3$ and 64° YX-$LiNbO_3$, respectively. We compute the center of the stopping band by averaging ω_s and ω_e on different mesh lengths and show the computational results in Table 3. Obviously, one can see that the central frequency monotonically converges to a constant when the mesh length is reduced. The numerical error from our finite element simulations is less than 0.2% and 1.2% for 36° YX-$LiTaO_3$ and 64° YX-$LiNbO_3$, respectively.

4.2. Comparison of Algorithm 1 and traditional Arnoldi method

From Tables 2 and 3, we have already shown that the accuracy of the computed eigenvalues and the central frequency of the stopping band obtained from the locally refined mesh with a mesh length of $p/80$ is almost the same as the values obtained from a uniform mesh with a mesh length of $p/160$. Therefore, in the following numerical computations, we consider only the coefficient matrices in the GEP (12) that are generated by the finite element discretization on the mesh that is locally refined twice over the uniform mesh with a mesh length of $p/80$.

Let the pair $(\lambda_{k,I}, \lambda_{k,O})$, $k = 1, \ldots, N$, denote the reciprocal pairs of eigenvalues of (12), where $\lambda_{k,I}$ and $\lambda_{k,O}$ lie inside and outside of $\mathbb{U}$, respectively. Fig. 5 displays the eigenvalues $\{\lambda_{1,I}, \ldots, \lambda_{9,I}, \lambda_{1,O}, \ldots, \lambda_{5,O}\}$ of the $LiNbO_3$ at a frequency of $\omega = 2.180$ GHz in which reciprocal pairs $(\lambda_{k,I}, \lambda_{k,O})$ for $k = 1, \ldots, 5$ close to $\mathbb{U}$ may be of interest. The notation $\mathbb{O}(\lambda)$ represents the set of all of the eigenvalues that cluster at the origin of the complex plane. Suppose that $2N$ eigenvalues near $\mathbb{U}$ are desired. The Arnoldi process in (21) and (22) for GTSHIRA is set to restart if the desired eigenpairs are not convergent when the dimension j of the subspace $\text{span}\{\widehat{Y}_j\}$ grows more than $5N$. The number for restarting the Arnoldi process is denoted by "#Iter" in the following.

A standard iterative approach for solving the GEP (12) is to apply the Arnoldi method on the equation directly. However, the reciprocal property of the eigenvalues is not guaranteed to be preserved in the computation. For Algorithm 1, based on the $(\mathcal{S} + \mathcal{S}^{-1})$-transform, if λ and μ are the eigenvalues of (12) and (17), respectively, then λ and μ satisfy the relationship $\mu = \lambda + \lambda^{-1}$. As a result, we can obtain the k-th reciprocal pair $(\lambda_{k,I}, \lambda_{k,O} \equiv 1/\lambda_{k,I})$ by solving the algebraic equation

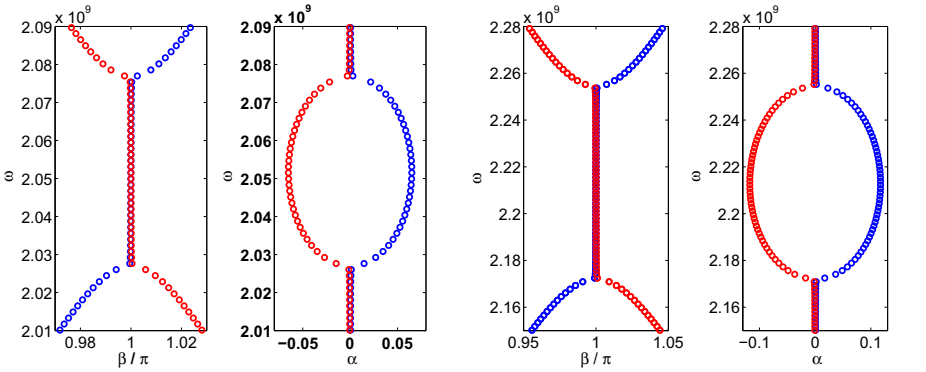

(a) Dispersion diagram of $LiTaO_3$ near the stopping band (b) Dispersion diagram of $LiNbO_3$ near the stopping band

Fig. 3. Dispersion diagrams.

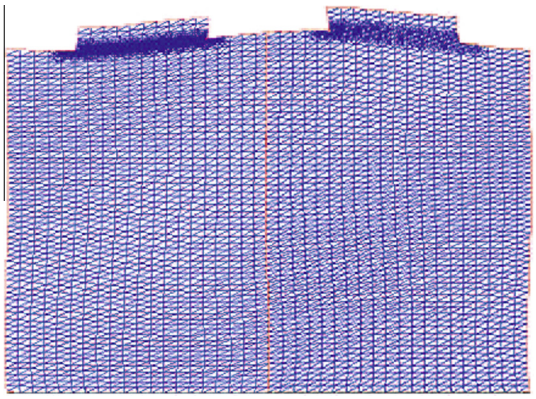

Fig. 4. A shear wave displacement.

Table 1
Dimension information of matrices M_1 and M_2 obtained from FEM discretization.

Mesh length	Uniform		Local refine	
	M_1	M_2	M_1	M_2
$p/20$	3554	183	4968	183
$p/40$	14,548	363	17,192	363
$p/80$	58,856	723	63,960	723
$p/160$	236,752	1443		

Table 2
The values of $|\lambda_{[16,u]} - \lambda_{[2^l,\xi]}|$ for different mesh lengths at frequencies ω_s and ω_e.

ω (GHz)	36° YX-$LiTaO_3$		64° YX-$LiNbO_3$	
	$\omega_s = 2.028$	$\omega_e = 2.075$	$\omega_s = 2.177$	$\omega_e = 2.257$
$\lvert\lambda_{[16,u]} - \lambda_{[2,u]}\rvert$	0.0222	0.0161	0.0955	0.0797
$\lvert\lambda_{[16,u]} - \lambda_{[2,\ell]}\rvert$	0.0178	0.0141	0.0857	0.0751
$\lvert\lambda_{[16,u]} - \lambda_{[4,u]}\rvert$	0.0076	0.0056	0.0299	0.0458
$\lvert\lambda_{[16,u]} - \lambda_{[4,\ell]}\rvert$	0.0036	0.0042	0.0166	0.0329
$\lvert\lambda_{[16,u]} - \lambda_{[8,u]}\rvert$	0.0016	0.0015	0.0060	0.0087
$\lvert\lambda_{[16,u]} - \lambda_{[8,\ell]}\rvert$	0.0001	0.0006	0.0007	0.0016

Table 3
Computed center frequency f_c (GHz) of stopping bands of LSAW on various meshes. Here, h_u and h_ℓ denote the mesh length of meshes without and with local refinement, respectively.

Mesh length		$h_u = \frac{p}{40}$	$h_\ell = \frac{p}{40}$	$h_u = \frac{p}{80}$	$h_\ell = \frac{p}{80}$	$h_u = \frac{p}{160}$
f_c	$LiTaO_3$	2.05246	2.05222	2.05206	2.05191	2.05183
	$LiNbO_3$	2.21623	2.21464	2.21385	2.21305	2.21305

$\mu_k = \lambda_{k,I} + \lambda_{k,I}^{-1}$ after the k-th eigenvalue μ_k of $\mathcal{K}z = \mu\mathcal{N}z$ is computed. Hence, the reciprocity is automatically preserved. Two numerical comparisons on preserving the reciprocal property, between Algorithm 1 and the traditional Arnoldi method, are listed in the following, where the eigenvalues of 64° YX-$LiNbO_3$ at a frequency of $\omega = 2.180$ GHz are computed.

- The traditional Arnoldi method does not guarantee that half of the computed eigenvalues lie inside of the unit circle and the others lie outside. For example, when we use the Arnoldi method to compute four eigenvalues (i.e., $2N = 4$) of (12) that are near to -1, the four convergent eigenvalues are $\lambda_{1,I}, \lambda_{1,O}, \lambda_{2,I}$ and $\lambda_{3,I}$. Clearly, the reciprocal property of the eigenvalues is lost.

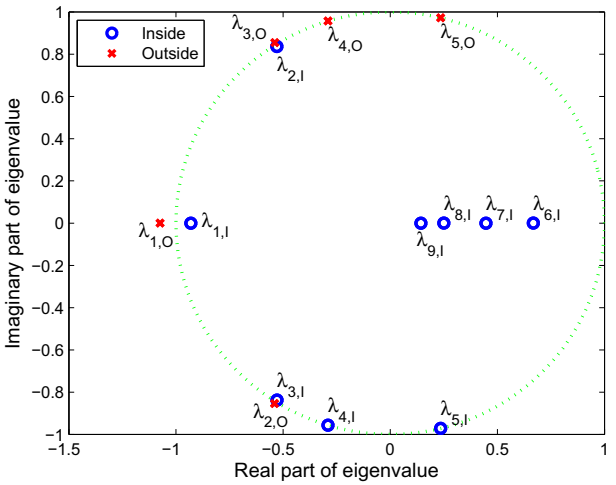

Fig. 5. Distribution of eigenvalues for 64° YX-$LiNbO_3$ at frequency 2.180 GHz.

- Suppose that one wants to compute the five reciprocal pairs $(\lambda_{k,I}, \lambda_{k,O})$ for $k = 1, \ldots, 5$ and takes a shift value $\tau = -2.89$. The eigenvalues in $\mathbb{O}(\lambda)$ are closer to τ than the eigenvalues $\lambda_{5,I}$ and $\lambda_{5,O}$. As a result, the desired reciprocal pair $(\lambda_{5,I}, \lambda_{5,O})$ near $\mathbb{U}$ cannot be discovered by the Arnoldi method. In contrast, in Algorithm 1, according to the relationship $\mu = \lambda + \lambda^{-1}$, the eigenvalue μ of $\mathcal{K}z = \mu\mathcal{N}z$ is far away from the shift value $\tau + 1/\tau$ when λ is close to the origin. Naturally, Algorithm 1 will not converge to those unwanted eigenvalues in $\mathbb{O}(\lambda)$. As a result, all of the desired eigenvalues can be discovered more easily by Algorithm 1 than with the traditional Arnoldi method. Our numerical results in Table 4 show that not only all of the desired eigenvalues are found by Algorithm 1, even when the number of desired eigenvalues is set to $2N = 18$, but Algorithm 1 also converges much faster than the traditional Arnoldi method. In fact, only two restarting steps are needed for Algorithm 1 to converge for all of the cases shown in Table 4. In addition, from the rightmost column of Table 4, one can see that all of the computed eigenvalues indeed preserve the reciprocal property. In contrast, the reciprocity of the convergent eigenvalues obtained by the Arnoldi method are diminished by approximately 3 significant digits.

From the above comparison, Algorithm 1 preserves the reciprocal property of the eigenvalues of the GEP (12) effectively. For measuring the accuracy of Algorithm 1, let us define the relative residual of an eigenpair (λ, u) of (12), where $u = [\psi_i, \psi_l]^\top$, as the following:

$$\frac{\left\| \begin{bmatrix} M_1 & G \\ F^\top & 0 \end{bmatrix} u - \lambda \begin{bmatrix} 0 & F \\ G^\top & M_2 \end{bmatrix} u \right\|_F}{\left\| \begin{bmatrix} M_1 & G \\ F^\top & 0 \end{bmatrix} \right\|_F \|u\|_F + |\lambda| \left\| \begin{bmatrix} 0 & F \\ G^\top & M_2 \end{bmatrix} \right\|_F \|u\|_F},$$

where $\|*\|_F$ is the Frobenius matrix norm. The maximal relative residuals of the 10 desired eigenpairs for 64° YX-$LiNbO_3$, with various frequencies, are shown in Fig. 6. From these numerical results, one can see that the eigenpairs produced by Algorithm 1 possess high accuracy in terms of the relative residual error.

Table 4
Convergent reciprocal pairs and the associated errors of reciprocity for 64° YX-$LiNbO_3$ at frequency 2.180 GHz versus different eigensolvers with various "2N" which denotes the number of interested eigenvalues. Here, $\tilde{\lambda}_k \in \mathbb{O}(\lambda)$ for $k = 1, \ldots, 4$.

Method	2N	Computed eigenvalues	#Iter	$\max\{\lvert\lambda_{k,I}\lambda_{k,O} - 1\rvert\}$
Arnoldi	8	$\{(\lambda_{k,I}, \lambda_{k,O})\}_{k=1}^4$	2	1.7×10^{-13}
	10	$\{(\lambda_{k,I}, \lambda_{k,O})\}_{k=1}^4$, $\{\tilde{\lambda}_k\}_{k=1}^2$	5	1.7×10^{-13}
	12	$\{(\lambda_{k,I}, \lambda_{k,O})\}_{k=1}^4$, $\{\tilde{\lambda}_k\}_{k=1}^4$	4	1.7×10^{-13}
Algorithm 1	8	$\{(\lambda_{k,I}, \lambda_{k,O})\}_{k=1}^4$	2	1.1×10^{-16}
	10	$\{(\lambda_{k,I}, \lambda_{k,O})\}_{k=1}^5$	2	1.1×10^{-16}
	12	$\{(\lambda_{k,I}, \lambda_{k,O})\}_{k=1}^6$	2	1.1×10^{-16}
	18	$\{(\lambda_{k,I}, \lambda_{k,O})\}_{k=1}^9$	2	2.2×10^{-16}

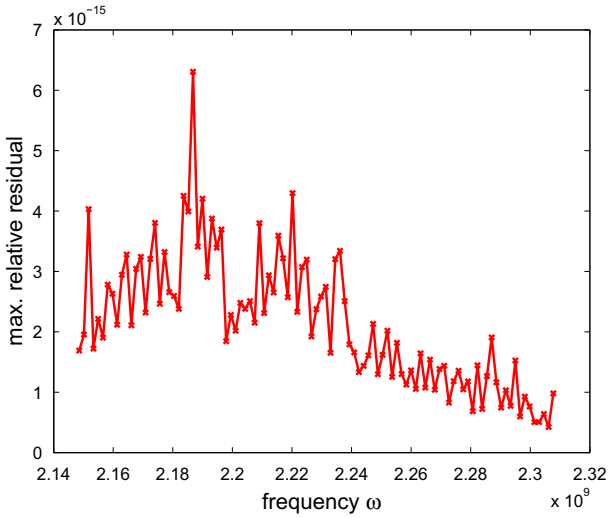

Fig. 6. Maximal relative residuals of the 10 desired eigenvalues produced by Algorithm 1.

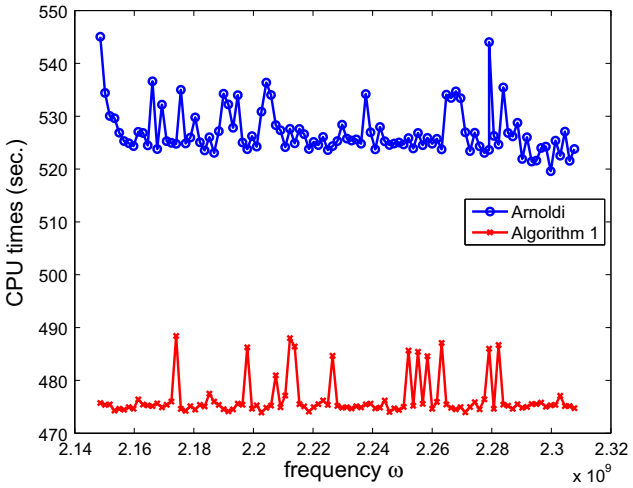

Fig. 7. CPU times for computing 10 desired eigenpairs by the traditional Arnoldi method and Algorithm 1.

Next, let us compare the efficiency of Algorithm 1 and the traditional Arnoldi method. The CPU times for computing 10 desired eigenpairs (i.e., $2N = 10$) for 64° YX-$LiNbO_3$ with various frequencies with Algorithm 1 and the traditional Arnoldi method are shown in Fig. 7. On average, Algorithm 1 takes only 476 s of CPU time to compute the desired eigenpairs for all of the frequencies ω in the search range. Obviously, the proposed algorithm is more efficient compared with the traditional Arnoldi method, which takes 527 s of CPU time to obtain all of the desired eigenpairs.

5. Conclusions

In this paper, we have modeled leaky surface acoustic wave propagation on a simple resonator with an interdigital transducer (IDT), where electrodes are arranged periodically on piezoelectric substrates (PZT) such as 64° YX-$LiNbO_3$ and 36° YX-$LiTaO_3$. The energy conservation Eq. (5) is discretized by a finite element method (FEM) applied to a single cell domain with proper periodic boundary conditions, as shown in Fig. 2. Eq. (5) is discretized on locally refined meshes to increase the accuracy of our numerical solutions. Our FEM simulation for predicting the center frequency of the stopping bands of the resonator is convergent and accurate with an error of approximately 1% compared with experimental data, as shown in Tables 2 and 3. For computing the dispersion diagram near the center of the stopping band of the resonator, we transform the GEP (12) into the TPQEP (3) to reveal the important reciprocal relationship of the eigenvalues in which the eigenvalues appear in

reciprocal pairs $(\lambda, 1/\lambda)$. The TPQEP (3) is then solved by GTSHIRA so that the reciprocal relationship of the eigenvalues can be automatically preserved. Our numerical results show that the traditional Arnoldi method converges slowly and fails to preserve the reciprocal property of the eigenvalues near the unit circle. In constrast, the proposed structure-preserving method in Algorithm 1 not only converges to those eigenpairs faster than does the traditional Arnoldi method, but it also possesses high accuracy in terms of the relative residual error. Furthermore, the reciprocal property of the eigenpairs is kept nicely under machine precision. Recently, some studies have been shown that the wave propagation speed in PZT can be affected by stress [26,27] and temperature [28]. With the proposed structure-preserving algorithm, we would like to investigate how the center and range of the SAW frequency changes under initial stress and thermal effect in our future studies.

Acknowledgments

This work is partially supported by the National Science Council and the National Center for Theoretical Sciences in Taiwan. The author C.T. Wu thanks the support from National Science Council in Taiwan under the Grant No. 99-2115-M-009-001.

References

[1] H. Allik, T. Hughes, Finite element method for piezoelectric vibration, Int. J. Numer. Methods Eng. 2 (1970) 151–157.
[2] M.B. Angel, M.I. Rocha-Gaso, M.I. Carmen, A.V. Antonio, Surface generated acoustic wave biosensors for detection of pathogens: a review, Sensors 9 (2009) 5740–5769.
[3] S.N. Atluri, M. Nakagaki, Computational methods for plane problems of fracture, in: Computational Method in Mechanics of Fracture, North-Holland Publishing Co., Amsterdam, 1986, pp. 170–227.
[4] B.A. Auld, Acoustic Fields and Waves in Solids, Krieger Publishing Company, Malabar, Florida, 1990.
[5] W. Bond, The mathematics of the physical properties of crystals, BSTJ 22 (1943) 1–72.
[6] M. Buchner, W. Ruile, A. Dietz, R. Dill, FEM analysis of the reflection coefficient of SAWS in an infinite periodic array, in: Proceedings of the IEEE Ultrasonics Symposium, 1991, pp. 371–375.
[7] C. Cai, H. Zheng, M.S. Khan, K.C. Hung, Modeling of material damping properties in ANSYS, in: International ANSYS Conference Proceedings, 2002.
[8] C.K. Campbell, Surface Acoustic Wave Devices for Mobile and Wireless Communications, Academic Press, INC., 1998.
[9] D.P. Chen, H.A. Haus, Analysis of metal-strip SAW gratings and transducers, IEEE Trans. Sonics Ultrason. 32 (3) (1985) 395–408.
[10] L.C. Chin, V.V. Vardan, V.K. Vardan, Hybrid finite element formulation for periodic piezoelectric arrays subjected to fluid loading, Int. J. Numer. Methods Eng. 37 (1994) 2987–3003.
[11] E.K.-W. Chu, T.-M. Hwang, W.-W. Lin, C.-T. Wu, Vibration of fast trains, palindromic eigenvalue problems and structure-preserving doubling algorithms, J. Comput. Appl. Math. 219 (2008) 237–252.
[12] P. Grisvard, Elliptic Problems in Nonsmooth Domains, Pitman Publishing INC., 1985.
[13] M. Hofer, N. Finger, G. Kovacs, J. Schöberl, S. Zaglmayr, U. Langer, R. Lerch, Finite-element simulation of wave propagation in periodic piezoelectric SAW structure, IEEE Trans. Ultrason. Ferroelectr. Freq. Control 53 (6) (2006) 1192–1201.
[14] T.-M. Huang, W.-W. Lin, J. Qian, Structure-preserving algorithms for palindromic quadratic eigenvalue problems arising from vibration on fast trains, SIAM J. Matrix Anal. Appl. 30 (2008) 1566–1592.
[15] C.F. Ipsen, Accurate eigenvalues for fast trains, SIAM News 37 (2004).
[16] M. Koshiba, S. Mitobe, M. Suzuki, Finite-element solution of periodic waveguides for acoustic waves, IEEE Trans. Ultrason. Ferroelectr. Freq. Control 34 (4) (1987) 472–477.
[17] J. Kushibiki, I. Takanaga, T. Sannomiya, Accurate measurements of the acoustical physical constants of $LiNbO_3$ and $LiTaO_3$ single crystals, IEEE Trans. Ultrason. Ferroelectr. Freq. Control 46 (1999) 1315–1323.
[18] R. Lerch, Simulation of piezoelectric devices by two- and three-dimensional finite elements, IEEE Trans. Ultrason. Ferroelectr. Freq. Control 37 (2) (1990) 1990.
[19] W.-W. Lin, A new method for computing the closed-loop eigenvalues of a discrete-time algebraic Riccatic equation, Linear Algebra Appl. 96 (1987) 157–180.
[20] J.E. San Miguel Medina, F. Buiochi, J.C. Adamowski, Numerical modeling of a circular piezoelectric ultrasonic transducer radiating in water, ABCM Symp. Ser. Mechatron. 2 (2006) 458–464.
[21] S. Mitobe, M. Koshiba, M. Suzuki, Theoretical determination of equivalent circuit parameters for reflective SAW metallic gratings, Electron. Commun. Jpn. 70 (6) (1987) 37–45.
[22] M. Mohamed, EL Gowini, W.A. Moussa, A finite element model of a MEMS-based surface acoustic wave hydrogen sensor, Sensors 10 (2010) 1232–1250.
[23] G. Nadar, E.C. Nelli Silva, J.C. Adamowski, Effective damping value of piezoelectric transducer determined by experimental techniques and numerical analysis, ABCM Symp. Ser. Mechatron. 1 (2004) 271–279.
[24] R.V. Patel, On computing the eigenvalues of a symplectic pencil, Linear Algebra Appl. 188 (1993) 591–611.
[25] U. Rösler, D. Cohrs, A. Dietz, G. Fisherauer, W. Ruile, P. Russer, R. Weigel. Determination of leaky saw propagation, reflection and coupling on $LiTaO_3$, in: IEEE Ultrasonics Symposium, 1995, pp. 247–250.
[26] A.M. Abd-Alla, S.M. Ahmed, Propagation of love waves in a non-homogeneous orthotropic elastic layer under initial stress overlying semi-infinite medium, Appl. Math. Comput. 106 (1999) 265–275.
[27] M.S. Son, Y.J. Kang, The effect of initial stress on the propagation behavior of SH waves in piezoelectric coupled plates, Ultrasonics 51 (4) (2011) 489–495.
[28] E. Bassiouny, Thermo-elastic behavior of thin sandwich panelmade of peizoelectric layers, Appl. Math. Comput. 218 (2012) 10009–10021.